NANO · MICRO small
www.small-journal.com

Donor:Acceptor Janus Nanoparticle-Based Films as Photoactive Layers: Control of Assembly and Impact on Performance of Devices

Yixuan Du, Yuemeng Wang, Volodymyr Shamraienko, Kathrin Pöschel, and Alla Synytska**

Water-processable organic semiconductor nanoparticles (NPs) are considered promising materials for the next-generation of optoelectronic applications due to their controlled size, internal structure, and environmentally friendly processing. Reasonably, the controllable assembly of donor:acceptor (D:A) NPs on large areas, quality, and packing density of deposited films, as well as layer morphology, will influence the effectiveness of charge transfer at an interface and the final performance of designed optoelectronic devices.This work represents an easy and effective approach for designing self-assembled monolayers of D:A NPs. In this self-assembly procedure, the NP arrays are prepared on a large scale (2×2 cm^2) at the air/water interface with controlled packing density and morphology. Due to the unique structure of individual D:A Janus particles and their assembled arrays, the Janus nanoparticle (JNP)-based device exhibits an 80% improvement of electron mobility and more balanced charge extraction compared to the conventional core–shell NP-based device. An outstanding performance of polymer solar cells with over 5% efficiency is achieved after post-annealing treatment of assembled arrays, representing one of the best results for NP-based organic photovoltaics. Ultimately, this work provides a new protocol for processing water-processable organic semiconductor colloids and future optoelectronic fabrication.

1. Introduction

Due to their mechanical flexibility, light weight, semi-transparency, and low-cost manufacturing via a roll-to-roll process, polymer solar cells (PSCs) can address the increasing global demand for renewable energy.[1,2] The deposition of the active layer in PSCs is generally processed with a halogenated solvent such as chloroform (CF), chlorobenzene (CB), and dichlorobenzene (DCB).[3–5] However, halogen atoms are detrimental to the human body and ecosystems; and therefore, substituting these toxic solvents is required for large-area fabrication and commercialization of PSCs.[6] The fabrication of semiconducting donor:acceptor (D:A) nanoparticles (NPs) dispersed in water offers a good solution to this issue[7,8] because it solves the problem of most organic photo-active donor/acceptor materials having low solubility in green solvents.[9] On the other hand, the donor/acceptor phase morphology can be designed and well-controlled on the nanoscale.[10] Excitons dissociation can occur at the donor/acceptor (D/A) interface within the NPs, enabling them to extract electrons/holes efficiently.[11]

Owing to their well-controlled internal nanostructures and environment-friendly processing, the aqueous D:A NP inks have been successfully applied to photocatalysis,[10–13] organic field-effect transistors,[14,15] photodetectors,[16] and photovoltaics.[17–19] However, the deposition of these aqueous NPs on substrates for applications remains a significant challenge. Generally, the most common approach is spin-coating. However, the concentration of D:A NP inks should be relatively high for this procedure (generally over 40 mg mL^{-1}).[18] However, the donor and acceptor materials are often wasted during the coated process, especially for water-processable NPs. Furthermore, the concentration of surfactants should also be well-controlled to achieve the high quality of the spin-coated layers. Too high or low concentration leads to pinholes in the deposited layer.[20] However, the remaining surfactants would affect the performance of the devices.[20] In addition, the spin-coating approach cannot meet different substrates and large-scale manufacture. More importantly, the packing density of particles and surface morphology of the NP layer cannot be controlled through the spin-coating technique.

Compared with spin-coating, air/water interfacial self-assembly is a simple, low-cost, and efficient approach to getting two-dimensional (2D) NP arrays.[21] Since Langmuir reported

Y. Du, Y. Wang, K. Pöschel, A. Synytska
Institut Physikalische Chemie und Physik der Polymere
Leibniz-Institut für Polymerforschung Dresden e.V.
Hohe Str. 6 01069, Dresden, Germany
E-mail: du@ipfdd.de; synytska@ipfdd.de
Y. Du, V. Shamraienko, A. Synytska
Fakultat Mathematik und Naturwissenschaften
Technische Universität Dresden
01062, Dresden, Germany
Y. Du, A. Synytska
Bayerisches Polymerinstitut
Universität Bayreuth
Universitätsstraße 30 95440, Bayreuth, Germany
The ORCID identification number(s) for the author(s) of this article can be found under https://doi.org/10.1002/smll.202206907.

DOI: 10.1002/smll.202206907

the transfer of molecules from a water surface onto a substrate in the 1920s,[22] this powerful technique has been successfully applied to get close-packed arrays for various inorganic nanoparticles[23–25] and organic nanoparticles.[23,26] The water surface offers an ideal soft platform for NPs to accumulate and self-assemble in this process.[27] The formed 2D nanoparticle arrays could be easily transferred onto desired substrates, whether hard, soft, or curved. More importantly, these packed nanoparticles can be designed in different patterns and then applied to optoelectronic devices.[28,29]

The packing pattern and morphology control of organic NP arrays can be achieved in this air/water assembly method. Importantly, the effects of packing density, high density of connection points between the individual nanoparticles, and their morphology on the final photoelectronic properties and performance of devices should be thoroughly investigated.

In this work, we prepared and assembled the organic homogeneously coated and Janus NPs consisting of polymer donor and fullerene acceptor at the air/water interface. These D:A nanoparticle arrays were designed in close-packed monolayers and deposited onto different substrates. Most importantly, the photoelectronic properties of obtained films varied by controlling their packing density and applying different structures of NPs from non-Janus to Janus. Last, the assembled NP films were fabricated as building blocks in optoelectronic devices, which brought out their competitive performance.

2. Results and Discussion

2.1. Overview of D:A NP Assembly at Air/Water Interface

First, the D:A nanoparticles (NPs) were fabricated via the mini-emulsion process as described elsewhere.[30,31] These water-processable NPs consisting of polymer donor poly[[4,8-bis[(2-ethylhexyl)oxy]benzo[1,2-b:4,5-b']dithiophene-2,6-diyl][3-fluoro-2-[(2-ethylhexyl)carbonyl]thieno[3,4-b]thiophenediyl]] (PTB7) were matched with the fullerene acceptor ([6,6]-Phenyl-C71-butyric acid methyl ester) ($PC_{71}BM$) (**Figure 1**a). The obtained NPs were monodispersed in a spherical structure, around 80 nm (Figure 1b). The NP dispersion was blue-grey and stable in the fridge for several months in the presence of surfactant sodium dodecyl sulfate (SDS) (Figure 1c).

In this work, the air/water interface assembly approach was applied to prepare donor:acceptor NP arrays comprised of homogeneously coated core–shell and Janus structured nanoparticles (Figure 1d). Briefly, the D:A NP dispersion was mixed with dispersant solvents and injected slowly onto the water surface. Following that, the D:A NPs remained on the water surface and were packed in sparse arrays after dispersant solvents evaporated. Next, additional butanol was injected onto the water surface to compress these sparse NPs into a densely packed array. Last, the close-packed NP films were transferred to the desired substrates (Figure 1d). The area of the floating film became smaller after the butanol addition, and the color was darker than before, as shown in the digital photos (Figure 1e). This indicates a closer packing of D:A Janus NP film. It is worth noting that this whole procedure could be finished in only a minute. The obtained NP films could be easily transferred onto hard (quartz glass and silicon wafer, Figure 1f,g), soft (filter paper and flexible polydimethylsiloxane (PDMS), Figure 1h,i), and even patterned polytetrafluoroethylene (PTFE) substrates (Figure 1j). This advantage exhibits the potential to meet different requirements in various applications.

2.2. Effects of Dispersants on Assembled NP Arrays

Dispersants are crucial in the air/water interfacial assembly process[25,32] because those solvents are applied to place NPs to the air/water interface and assist the absorption of particles at the interface.[21] Usually, dispersants have a high evaporation rate and lower density than water, ensuring the solvents spread on the water surface and evaporate afterward. Therefore, five different dispersed solvents, methanol, ethanol, isopropanol (IPA), 1-butanol, and acetone, were investigated to disperse D:A NPs in this research (Figure S1, Supporting Information).

The PTB7:$PC_{71}BM$ NPs were packed in a multi-layer from acetone dispersions, as shown in the scanning electron microscope (SEM) images (Figure S1e, Supporting Information). Similarly, the NP film obtained from methanol showed many aggregated NPs (Figure S1a, Supporting Information). This indicates that the surface charge of most particles is destroyed in acetone and methanol solvents, resulting in aggregated particles and assembled blocks. On the other hand, the D:A NPs were packed in a monolayer when we applied ethanol, IPA, and butanol as dispersed solvents. However, the obtained monolayer has many non-closed areas, resulting in a net-like structure (Figure S1, Supporting Information). The vacancy holes were smaller when butanol was applied as a dispersed solvent rather than ethanol or IPA (Figure S1b–d, Supporting Information). It is also worth noting that PTB7:$PC_{71}BM$ NPs tend to aggregate in ethanol and IPA; and therefore, the filter process is essential before adding the dispersion to water.

2.3. Effects of Surfactants on the NP Floating Procedure

In addition, the surfactant (SDS in this work) dramatically affects surface charge; and thus, the quality of the self-assembled NP layer. Therefore, we applied centrifugal dialysis to remove the residual surfactants in the dispersion before assembly. Monitoring the surfactant concentration is necessary to understand the centrifugal dialysis process and the following assembly procedure. First, we measured the equilibrium surface tension (γ) of a series of SDS water solutions with different concentrations (Figure S2a, Supporting Information). Data are shown in Table S1, Supporting Information, and plotted in Figure S2, Supporting Information, where surface tension values for 17 different concentrations are shown. As expected, a steep drop in the surface tension occurred as SDS concentration increased before critical micelle concentration (CMC) (Figure S2a, Supporting Information). On the other hand, when the concentration was higher than CMC (8.2 mM), the SDS concentration weakly affected the equilibrium surface tension, from 38.36 to 36.43 mN m^{-1} (Table S1, Supporting Information). A dependence was found between concentration (c) of SDS (<8.2 mM) and the

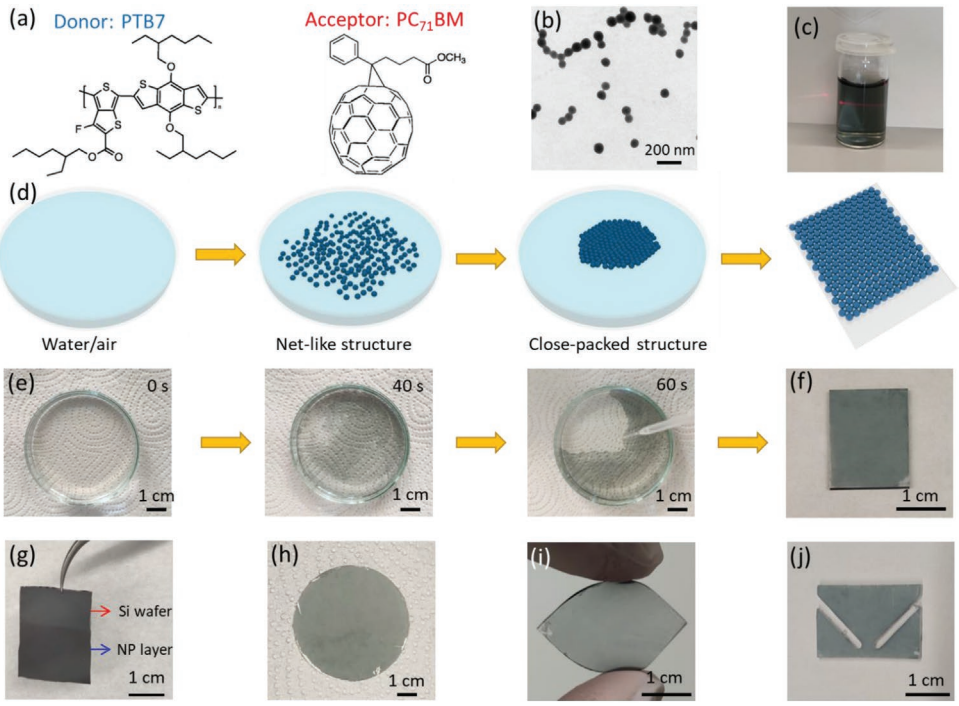

Figure 1. a) Chemical structures of PTB7 (donor) and $PC_{71}BM$ (acceptor). b) Bright-field TEM image of PTB7:$PC_{71}BM$ NPs. c) Tyndall effect shown in PTB7:$PC_{71}BM$ NP dispersion. d) Schematic representation of fabrication of hexagonal close-packed PTB7:$PC_{71}BM$ NP films on the water surface and transfer to target substrates. e) Digital photos of the PTB7:$PC_{71}BM$ NP array, showing the transition from net-like structure to a close-packed structure at air/water interface by dropping butanol onto the water surface. Transferred PTB7:$PC_{71}BM$ NP film on various substrates: f) quartz glass, g) silicon wafer, h) filter paper, i) flexible PDMS, and j) patterned PTFE.

equilibrium surface tension, as shown in Figure S2b, Supporting Information; Equation (1) as follows:

$$\gamma = 50.14 \times e^{-c/7.26} + 22.32 \quad (1)$$

To quantitatively investigate SDS concentration after washing, the equilibrium surface tension of dispersion was measured in this work. **Figure 2**c presents the equilibrium surface tension curve for NP dispersion as a function of centrifugal dialysis steps. The surface tension changed negligibly after four washing steps, from 36.55 to 37.49 mN m^{-1}. This was because the concentration of residual surfactant was still higher than its CMC. In contrast, the surface tension increased dramatically from 39.29 mN m^{-1} after five washing steps to 69.80 mN m^{-1} after eight washing times. The residual SDS concentrations were calculated according to Equation (1) and summarized in Table S2, Supporting Information. This study concludes that most surfactants are stripped after dialysis eight times, and the SDS concentration drops from 34.2 to 0.4 mM (Table S2, Supporting Information).

Next, we studied the relationship between centrifugal dialysis and floating performance. Here, PTB7:$PC_{71}BM$ NPs with different washing steps was transferred from dispersion (1 mg mL^{-1}) to the air/water interface (Figure 2a). As seen from the digital photos, the floating area of NPs became larger and fewer particles were submerged in water with increasing washing steps (Figure 2b). It suggests that the floating procedure is closely related to the concentration of residual surfactants (Figure 2c). The SDS molecules increase the solubility of butanol with water. It results that the NPs are easily submerged into the water phase when SDS concentration is high. Thus, fewer particles are left on the water surface, resulting in a low floating yield. The further SEM results support that the floating area of NP films is tightly related to number of washing times (Figure S3, Supporting Information). Therefore, more floating D:A NPs were obtained when we applied more dialysis steps to remove surfactants.

To quantitatively study the performance of this procedure, we aimed to evaluate the floating yield of dropped NPs. It can be calculated by measuring the ratio of the NPs submerged in the water phase. In detail, the floating yield (Y) of the D:A particles can be obtained from the following Equation (2):[23]

$$Y = 1 - \left(\frac{C \times V}{C_0 \times V_0}\right) = 1 - \left(\frac{A \times V}{A_0 \times V_0}\right) \quad (2)$$

where C and C_0 refer to the particle concentration in the water phase after transfer and the initial NP suspension; V and V_0 represent the volume of the bottom water phase and the initial dispersion drop; and A and A_0 are the absorbances corresponding to the concentration.

The UV–vis absorbance of varied NP concentrations in water is reported in Figure S4a, Supporting Information. According to the Beer–Lambert law,[33] the scattering intensity of the suspension is linearly proportional to nanoparticle concentration.[34] As shown in the figure, the absorbance at 240 nm is linearly increased with the PTB7:$PC_{71}BM$ NPs concentration (Figure S4b, Supporting Information).

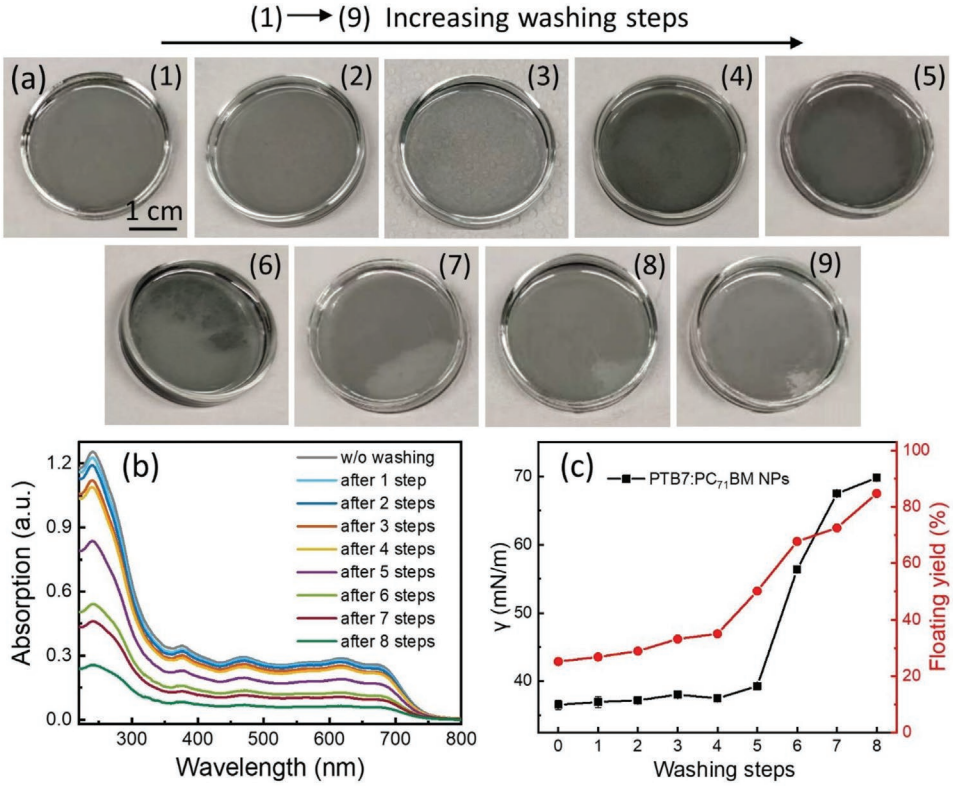

Figure 2. a) Photographs of the area occupied by the floating PTB7:$PC_{71}BM$ particles at the air/water interface as an increasing number of centrifugal dialysis. b) UV–vis absorbance spectra measured from the water phase after transferring the floating particles as a function of washing step. c) Surface tension (black line) and floating yield (red line) of the D:A nanoparticles according to various washing steps.

The UV–vis absorbance of D:A particles in the water phase was dramatically decreased by the increased washing steps (Figure 2b). Here, we also chose their absorbance at 240 nm to calculate the corresponding floating yield (Equation (2)). It can be concluded that the yield of the PTB7:$PC_{71}BM$ particles floating at the air/water interface is continuously increased by increasing centrifugal dialysis steps (Figure 2c; Table S3, Supporting Information). Last, the floating yield of the D:A nanoparticles reached 85% after eight washing times (Table S3, Supporting Information).

2.4. Assembly Strategies for the Fabrication of Densely-Packed NP Films

Designing more densely-packed D:A NPs arrays is crucial to obtain more sunlight absorption and efficient charge extraction from the D/A interface, resulting in higher-performance devices. Therefore, the further strategy was attempted to prepare closed-packed D:A NP film at a liquid/liquid (hexane/water) interface. The NPs were highly mobile at the hexane/water interface, leading to a homogeneous coverage of the interface; and thus, the reduction in structural defects.[27,35] When the top phase liquid (hexane) evaporated slowly, the water/oil interface areadecreased, causing densely packed NPs.[36,37] In this experiment, the floating NP film at the hexane/water interface was smaller than that at the air/water interface (Figure S5a,b, Supporting Information), which indicates the closer packed NP array. Moreover, the obtained film at the hexane/water interface was continuous without apparent cracks.

Interestingly, the film color changed from grey blue to sky blue, close to pure PTB7 NP film (Figure S5a,b, Supporting Information). Therefore, we assumed that the $PC_{71}BM$ component was dissolved in the hexane phase, and the following UV–vis absorption spectra proved this to be true (Figure S5c–e, Supporting Information). There was no change in the characteristic peak positions of PTB7 NP film, only higher absorption intensity between the two different interface assembly methods (Figure S5c, Supporting Information). However, the characteristic peaks of $PC_{71}BM$ disappeared in pure $PC_{71}BM$ NP film and PTB7:$PC_{71}BM$ NP film (Figure S5d,e, Supporting Information).

As proved by electron microscopy, the NPs were packed much closer after involving the hexane phase (Figure S6, Supporting Information). However, the particles were interconnected, and we could not distinguish the individual particle. Therefore, we concluded that the $PC_{71}BM$ might be dissolved in the upper hexane phase. Although the close-packed and homogenous NP film was successfully obtained, the hexane/water interfacial assembly was unsuitable for fullerene-contained systems.

Butanol was added to prepare the close-packed monolayer in the following experiments. The butanol drop spread quickly on the water surface and pushed the floating NPs toward the edge of the container. In detail, the interfacial tension results showed a considerable difference between the air/water interface (72.8 mN m^{-1}) and the butanol/water interface

(22.9 mN m^{-1}) (**Figure 3**a). This surface tension difference made the NPs migrate toward the higher tension area; thus, forming a dense NP monolayer.[38] Therefore, the PTB7:$PC_{71}BM$ NP film transformed from a net-like structure (Figure 3b) to a hexagonal close-packed structure[39,40] (Figure 3c) after the addition of butanol onto the water surface. Subsequently, the UV–vis absorption and photoluminescence (PL) intensity of the film were enhanced after NPs compression (Figure 3d). Moreover, the film color became darker after compression, obtained from digital photos (inset figure in Figure 3d). As expected, the net-like film showed a≈116° water contact angle (Figure 3e), while the close-packed NP film possessed a more hydrophobic surface (136.5° water contact angle, Figure 3f) due to the densely packed structure.

The excess surfactants in the active layer would affect the charge transport, resulting in poor performance.[14,17] Therefore, a washing procedure is necessary to remove these excess surfactants. Typically, the transferred NP layer was annealed at 140 °C for 10 min and then dipped in a water/alcohol mixture for 30 min to wash off surfactants.[9,41] We compared the water contact angles between washed and unwashed NP layers (Figure S7, Supporting Information) and found that the angle of the NP layer measured after washing was identical to that of the as-prepared film. This interfacial assembly process indicates no residual surfactants left in NP films.

2.5. Fabrication and Investigation of NP Films With Different Internal Structures

In our previous work, high-quality pure PTB7, pure $PC_{71}BM$, PTB7:$PC_{71}BM$ core–shell, and Janus NPs were synthesized.[31] To prove the universality of our self-assembly strategy, these two different NPs ($PC_{71}BM$-core:PTB7-shell ($PC_{71}BM$-c:PTB7-s) NPs and PTB7:$PC_{71}BM$ Janus NPs) and pure donor/acceptor NPs (PTB7 NPs and $PC_{71}BM$ NPs) were performed to apply this method afterward (Figure S8, Supporting Information).

The results prove these four kinds of NPs can be arrayed in a close-packed monolayer. Furthermore, energy-filtered transmission electron microscopy (EF-TEM) delivered information about their different internal morphology based on detecting carbon (C) and sulfur (S) elements. The apparent contrast between donor and acceptor domains is shown by selectively recording the energy losses of desired elements. The sulfur element exists in PTB7, while there is no sulfur in $PC_{71}BM$ (Figure 1a). Therefore, the EF-TEM technique is an effective way to distinguish core–shell (Figure S8c, Supporting Information) and Janus (Figure S8d, Supporting Information) structures. In addition, various kinds of NP films were in close-packed monolayer and exhibited the enhancement of UV–vis absorption and PL intensity after butanol compression (Figure S9, Supporting Information).

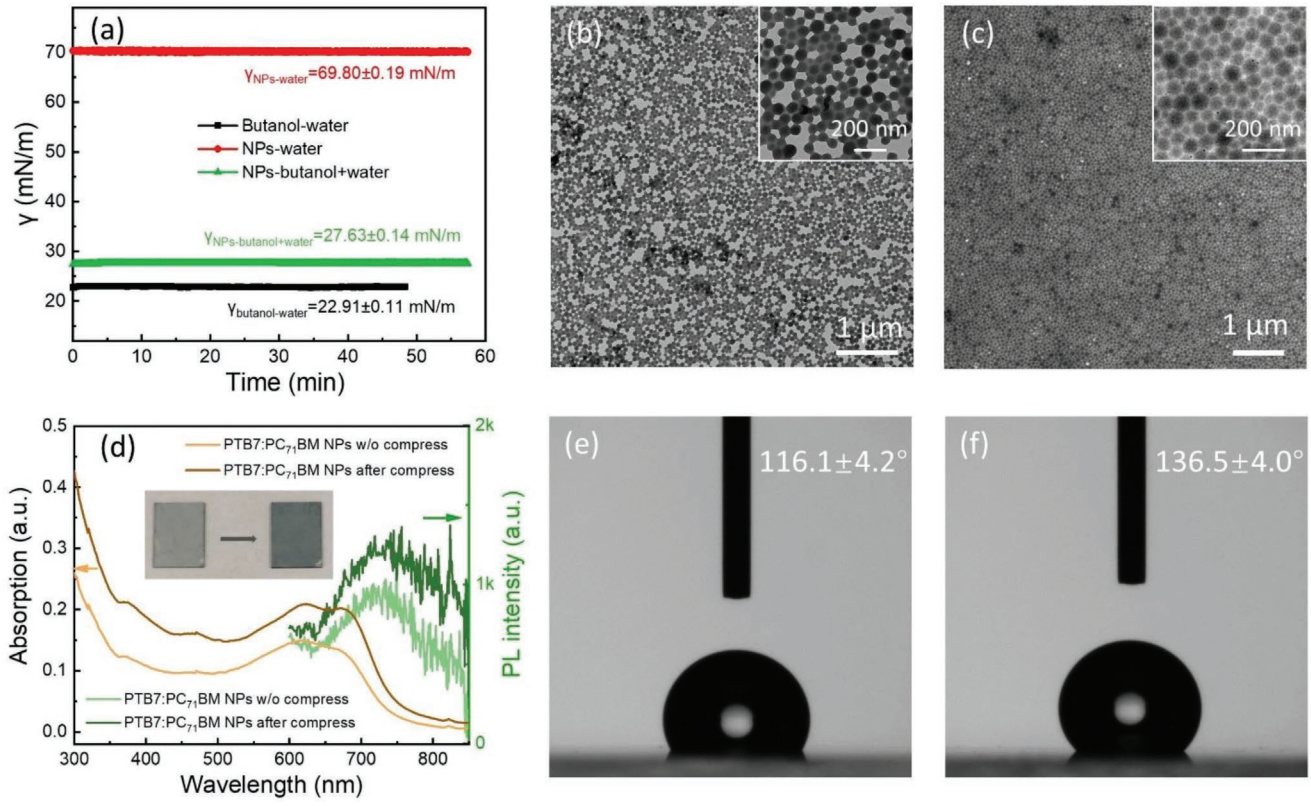

Figure 3. a) Interfacial tension of PTB7:$PC_{71}BM$ NPs at the air/water interface (NPs concentration = 1 mg mL^{-1}). Representative bright-field TEM images of PTB7:$PC_{71}BM$ NP film b) in a net-like structure before compression and c) in a close-packed structure after compression (inset: magnified area). d) UV–vis absorption and steady-state photoluminescence (PL) of PTB7:$PC_{71}BM$ NP films in net-like and close-packed structures (inset: digital photos of NP films on quartz glass). Water wetting property of the surface of the PTB7:$PC_{71}BM$ NPs in e) net-like structure and f) close-packed structure.

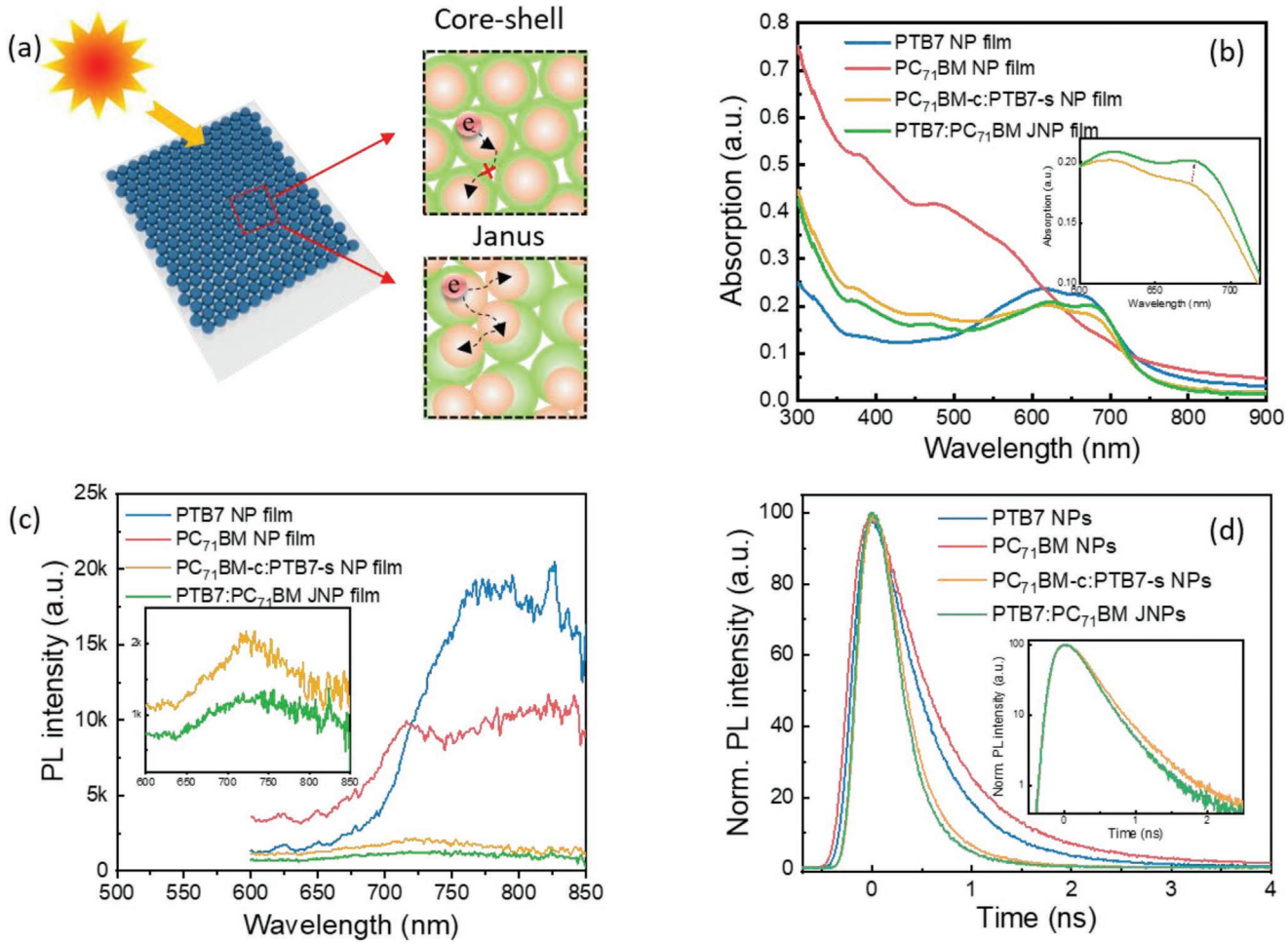

Figure 4. a) Scheme of the electron transport inside of PTB7:$PC_{71}BM$ core–shell NP and Janus NP films in hexagonal close-packed structure. b) UV–vis absorption spectra, c) steady-state PL spectra, and d) time-correlated single-photon counting (TCSPC) emission traces of pure PTB7 NP, $PC_{71}BM$ NP, $PC_{71}BM$-c:PTB7-s NP, and PTB7:$PC_{71}BM$ Janus NP films (inset: magnified data without pure PTB7 and $PC_{71}BM$ NP films).

Due to the heterojunction structure of D:A NPs, electrons/holes can be generated and transferred inside of D:A NPs after sunlight absorption. As proved in previous studies, their different internal structures result in different optical and charge generation/transfer properties.[10] For the core–shell NP film, the generated charges can only transport inside particles due to the confined structure. In contrast, the electrons can be transported to neighbor particles in Janus nanoparticle (JNP)-based film due to the continuous acceptor domains (**Figure 4**a).

Next, the absorption properties of NP films based on different structured NPs were studied by UV–vis spectrophotometry (Figure 4b). The pure $PC_{71}BM$ NPs film showed characteristic peaks at 370 and 480 nm, whereas the characteristic peaks of PTB7 NPs film were around 607 and 670 nm (Figure 4b). Furthermore, the absorption spectra between $PC_{71}BM$-c:PTB7-s NP and PTB7:$PC_{71}BM$ JNP based films showed similar characteristic peaks. However, Janus nanoparticle film exhibited a more substantial shoulder peak (around 670 nm, inset figure in Figure 4b), which could be ascribed to different semi-crystalline PTB7 domains.

The photoluminescence(PL) emission peaks of pure PTB7 and $PC_{71}BM$ NPs were around 778 and 717 nm, respectively (Figure 4c). However, excellent PL quenching was observed for $PC_{71}BM$-c:PTB7-s and PTB7:$PC_{71}BM$ Janus NP films. This could be ascribed to forming of a large-area interface between the donor and acceptor phases. In addition, Janus NP film exhibited a more obvious PL quenching than core–shell NPs, indicating a more efficient energy transfer behavior (inset figure in Figure 4c).

To further study the charge transfer properties in obtained D:A NP films, time-resolved photoluminescence (TR-PL) measurement was performed among various films (Figure 4d). All the obtained TR-PL decay curves could be well fitted to a bi-exponential decay function, consisting of the fast (τ_1) and slow (τ_2) lifetime components (**Table 1**). For pure PTB7 NP and $PC_{71}BM$ NP films, the fluorescence lifetime (τ) was calculated as 0.705 and 0.946 ns, respectively. Obviously, the decay time was dramatically shortened in PTB7:$PC_{71}BM$ core–shell and Janus NP films (Figure 4d). The Janus NP film exhibited a shorter fluorescence lifetime (0.355 ns) compared to the core–shell structure (0.415 ns) (inset figure in Figure 4d). The Janus NP

Table 1. Decay time constants and amplitudes from time-resolved decay traces of assembled NP films.

NP films	A_1	τ_1 [ns]	A_2	τ_2 [ns]	χ^{2*}	τ_{avg} [ns]
$PC_{71}BM$	12.800 ± 0.040	0.5892 ± 0.003	1.250 ± 0.048	2.020 ± 0.037	1.070	0.946 ± 0.005
PTB7	9.280 ± 0.029	0.503 ± 0.003	0.423 ± 0.027	1.880 ± 0.067	1.040	0.705 ± 0.006
$PC_{71}BM$-c:PTB7-s	6.450 ± 0.033	0.282 ± 0.002	0.101 ± 0.024	1.800 ± 0.260	1.080	0.415 ± 0.019
PTB7:$PC_{71}BM$ Janus	7.980 ± 0.096	0.256 ± 0.008	0.490 ± 0.150	0.840 ± 0.130	1.122	0.355 ± 0.009

film also consistently showed the most effective PL quenching (Figure 4c). The fluorescence lifetime was related to the exciton diffusion and charge transfer processes.[42] In detail, the fast decay τ_1 could be attributed to non-radiative decay, which originated from the charge extraction within the NP film.[43] On the other hand, τ_2 was related to the radiative recombination of free charge carriers within the D:A NP film.[44] For the Janus NP film, both τ_1 and τ_2 were dramatically shortened to 0.256 and 0.840 ns, respectively. This indicates a more efficient charge extraction in the Janus NP system. Therefore, Janus NP-based film had a higher charge diffusion and transfer rate, reducing geminate charge recombination. This result also suggests that the charge transfer efficiency depends on the internal structure of the D:A nanoparticles.[45]

2.6. Investigation of Donor:Acceptor NP Films in Optoelectronic Applications

Last, to investigate the D:A NP films in applications, we fabricated polymer solar cells (PSCs) using an inverted device architecture. The devices were comprised of indium tin oxide (ITO)/zinc oxide (ZnO)/D:A NP film/molybdenum trioxide (MoO_3)/silver (Ag) anode (**Figure 5**a). In addition, the bulk heterojunction (BHJ) structured solar cells formed by spin-coating from DCB solutions under the ambient atmosphere were also prepared as a reference. Their performances were studied by the fabricated PSC devices under illumination at AM 1.5G (100 mW*cm^{-2}).

The current density–voltage (J–V) curves of the NPs and BHJ structured PSCs are depicted (Figure 5b,c) with the key performance parameters (**Table 2**). The PTB7:$PC_{71}BM$ JNP-based devices exhibited much higher power conversion efficiency (PCE) values (3.35%) than core–shell NP-based devices (2.17%), which could be attributed to their efficient charge transfer, explained in Figure 4.

In addition, we applied poly[4,8-bis(5-(2-ethylhexyl)thiophene-2-yl)benzo[1,2-b;4,5-b']dithiophene-2,6-diyl-alt-(4-(2-ethylhexyl)-3-fluorothieno[3,4b] thiophene-)-2-carboxylate-2-6-diyl)] (PTB7-Th) instead of PTB7 as the donor polymer. The PTB7-Th Janus NP devices exhibited excellent performance (best PCE: 5.11%), achieving one of the best efficiency rates among NP-based organic photovoltaics. Among device parameters, the Janus NP device's short-circuit current density (J_{SC}) was highly improved. At the same time, open-circuit voltage (V_{OC}) was constant, indicating the efficient charge transfer of Janus NPs at D/A interfaces. We conducted long-term stability tests on the NP film-based devices without encapsulation under ambient conditions (Figure 5d). These devices remained at ≈90% of their initial PCE after a month, indicating their high stability in the air.

Table S4, Supporting Information, shows the photovoltaic performance of devices based on non-close packed NP layers. The assembled NP layer without compression has many defects as shown in Figure 3b. These defects in the photoactive layer will result in low performance (PCE: 0.256%). In addition, the defects also result in the poor stability of devices. The PCE is only 52% of the original device after 30 days.

2.7. Investigation of Charge Mobility in NP-Based Solar Cells

To further investigate the effects of NP structure on charge transport in fabricated devices, the charge carrier mobilities were estimated using the space-charge limited current (SCLC) model based on the Mott–Gurney law equation[46] (**Figure 6**):

$$J_{SCL} = \frac{9}{8}\varepsilon\varepsilon\varepsilon_0\mu\frac{V^2}{d^3} \quad (3)$$

where $\epsilon \approx 3$ is the organic film relative dielectric constant, ϵ_0 is the vacuum dielectric constant of 8.85×10^{-12} F m^{-1}, μ refers to the charge carrier mobility, and d represents the film thickness.[46] The thickness of photoactive layer was characterized by 3D scandisk confocal microscope (Figures S11 and S12, Supporting Information). The hole mobility in the core–shell NP device was generally consistent with the Janus particle device (Table S5, Supporting Information). In contrast, the PTB7:$PC_{71}BM$ JNP device exhibited much higher electron mobility (6.21×10^{-5} cm^2*V^{-1}*s^{-1}) than the core–shell NP device (3.37×10^{-5} cm^2*V^{-1}*s^{-1}). It could be attributed to the confined acceptor phase in core–shell NPs. This confined structure prevents the transfer and extraction of electrons in core–shell NP based devices. On the other side, the D:A NP Janus NP had a certain phase separation, which facilitated the charge transfer. The improved electron mobility and more balanced charge mobility in the Janus NP based devices suggestbetter percolation pathways for the charge carriers.[47] Therefore, it results in enhanced charge extraction efficiency, fill factor; and thus, reduced charge recombination.[48]

2.8. Optimization of Assembled NP Based Devices

Thermal annealing treatment is a usual procedure to improve the performance of NP-based PSC devices. It can result in the homogenous film from the isolated particles by post-annealing treatment. Therefore, a varied annealing temperature study was

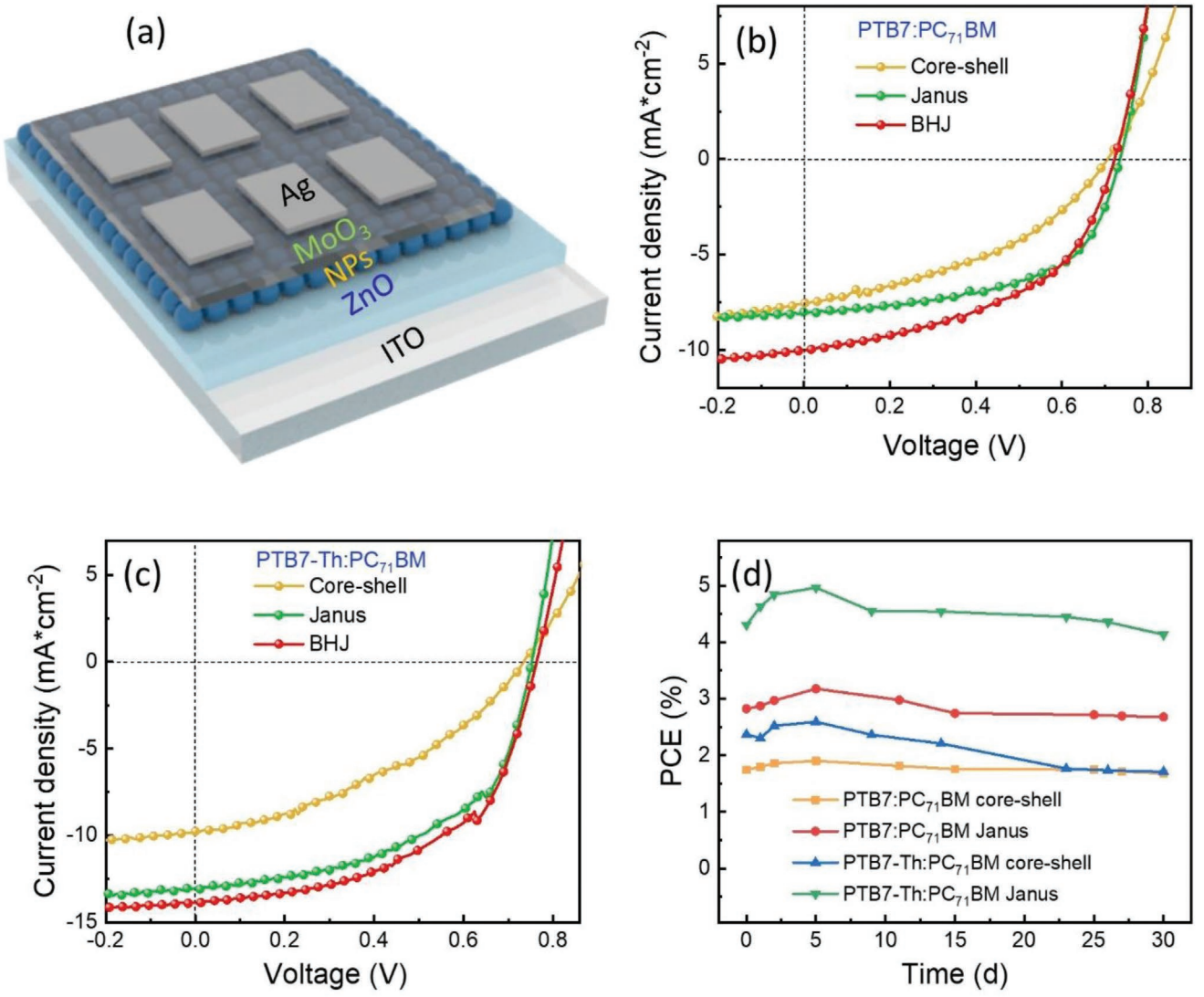

Figure 5. a) Device architecture of NP film-based polymer solar cells in this work. *J–V* curves of the devices in b) PTB7:PC_{71}BM and c) PTB7-Th:PC_{71}BM NP-based PSCs; comparison to those of reference devices fabricated from dichlorobenzene. d) Stability of unencapsulated devices based on donor:acceptor NPs. All devices were stored and measured under ambient conditions without encapsulation.

conducted, with PTB7:PC_{71}BM Janus NP device data summarized in Figure S13, Supporting Information; **Table 3**.

The PCE of PTB7:PC_{71}BM JNP devices was enhanced from 0.75% to 2.82% by 140 °C annealing treatment for 10 min (Table 3). This obtained result suggests that the proper thermal treatment was attributed to overcoming the efficiency limit in the PTB7:PC_{71}BM JNP based devices. However, the PSC device performance dropped sharply with raising annealing temperature (above 160 °C), reaching a PCE of 1.76% at the 200 °C annealing temperature. The reduction in NP PSC device

Table 2. Summary of the photovoltaic performance of PTB7/PTB7-Th:PC_{71}BM based devices in different structures.

Structures	Solvents	V_{oc} [V]	J_{sc} [mA cm^{-2}]	FF [%]	PCE [%]	Best PCE [%]
PC_{71}BM-c:PTB7-s NPs	Water	0.69 ± 0.02	7.08 ± 0.54	35.17 ± 4.27	1.74 ± 0.31	2.17
PTB7:PC_{71}BM Janus NPs	Water	0.74 ± 0.02	7.93 ± 0.73	48.52 ± 7.78	2.82 ± 0.47	3.35
PTB7:PC_{71}BM BHJ	o-DCB	0.72 ± 0.01	9.40 ± 0.40	49.08 ± 1.87	3.32 ± 0.11	3.51
PC_{71}BM-c:PTB7-Th-s NPs	Water	0.72 ± 0.02	8.85 ± 1.03	36.40 ± 3.83	2.37 ± 0.55	3.16
PTB7-Th:PC_{71}BM Janus NPs	Water	0.74 ± 0.03	12.59 ± 0.39	45.68 ± 6.86	4.31 ± 0.80	5.11
PTB7-Th:PC_{71}BM BHJ	o-DCB	0.76 ± 0.01	13.91 ± 0.12	53.01 ± 0.54	5.62 ± 0.07	5.73

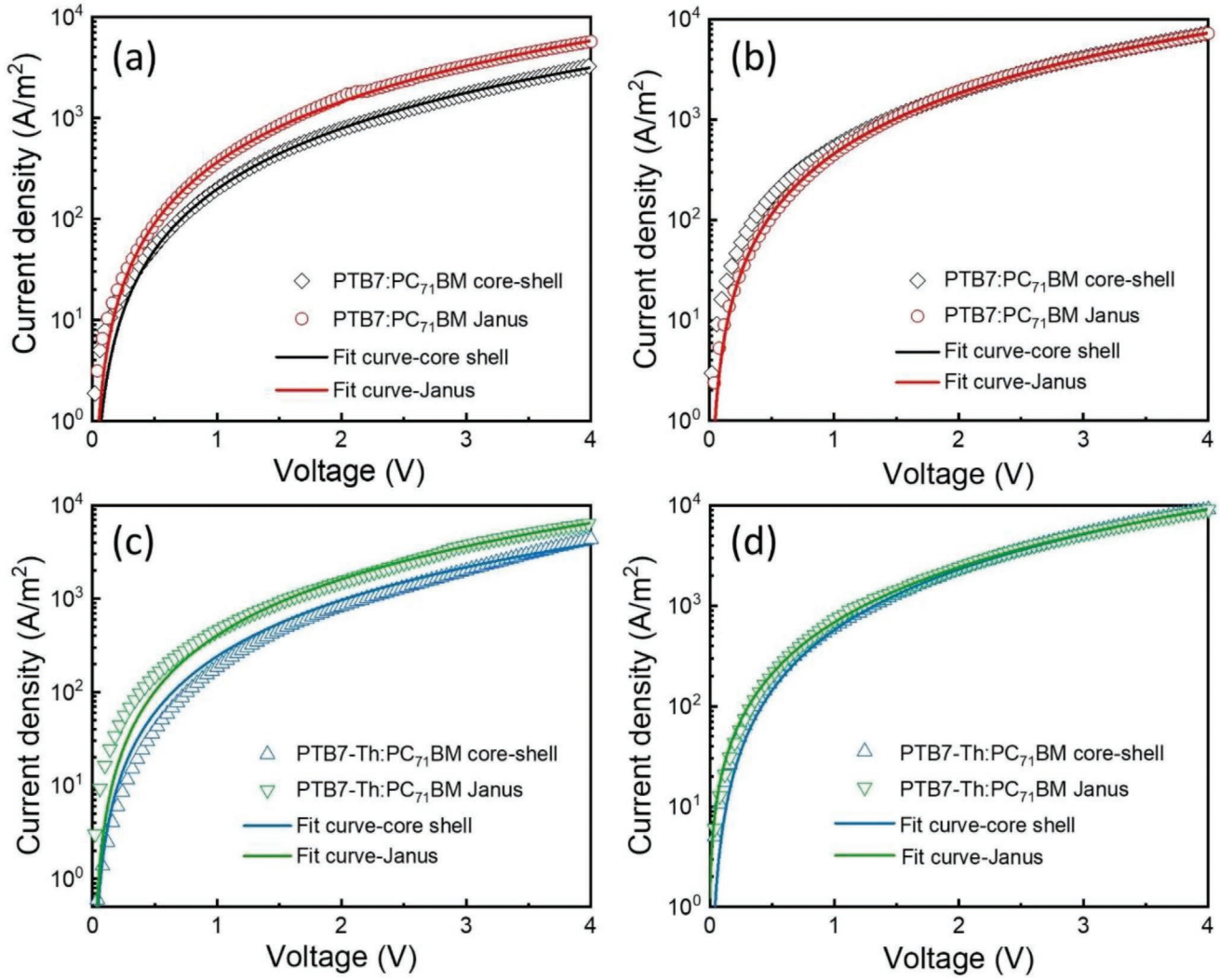

Figure 6. Dark *J*–*V* characteristics of PTB7:$PC_{71}BM$ NP based a) electron-only and b) hole-only devices; PTB7-Th:$PC_{71}BM$ NP based c) electron-only and d) hole-only devices. Electron-only device structure: glass/ITO/ZnO/NP film/aluminum (Al); hole-only device structure: glass/ITO/MoO_3/NP film/MoO_3/Ag.

performance when annealing temperatures exceeded 160 °C was in agreement with the glass transition temperature (T_g) of fullerene $PC_{71}BM$ (163 °C).[49] It indicates a morphological transition of the NP layer when the temperature is above 160 °C.

Next, the absorption properties of PTB7:$PC_{71}BM$ JNP films under various annealing conditions were studied by UV–vis spectrophotometry (Figure S14, Supporting Information). The characteristic peaks of PTB7 (607 and 670 nm) were enhanced with increased annealing temperatures (Figure S14a, Supporting Information). This change could be ascribed to different semi-crystalline polymer PTB7 domains and the aggregation of particles with raising annealing temperatures. We also noted that

Table 3. Summary of the photovoltaic performance of PTB7:$PC_{71}BM$ NP-based devices under various annealing temperatures.

Annealing temperature [°C]	V_{oc} [V]	J_{sc} [mA cm^{-2}]	FF [%]	PCE [%]	Best PCE [%]
w/o	0.65 ± 0.37	4.65 ± 2.65	25.70 ± 6.37	0.75 ± 0.45	1.40
80	0.57 ± 0.25	6.80 ± 2.24	37.17 ± 7.67	1.77 ± 0.85	2.70
110	0.68 ± 0.04	6.77 ± 0.69	46.35 ± 6.36	2.16 ± 0.43	2.63
140	0.74 ± 0.02	7.93 ± 0.73	48.52 ± 7.78	2.82 ± 0.47	3.35
170	0.70 ± 0.02	7.21 ± 1.81	43.86 ± 5.33	2.31 ± 0.87	3.32
200	0.67 ± 0.04	4.95 ± 1.13	36.41 ± 6.15	1.28 ± 0.44	1.76

the dramatic PL quenching was observed for the PTB7:$PC_{71}BM$ Janus NP film when the annealing temperature was applied at 140 °C. It was ascribed to forming a large-area interface between the donor and acceptor phase because the PTB7 and $PC_{71}BM$ domains were merged into each other after annealing (Figure S14b, Supporting Information). This PL quenching study further supported that the post-annealing process could improve the charge separation behavior of the NP based films.

To further study the charge transfer properties in obtained donor:acceptor NP films, the TR-PL study was subsequently performed (Figure S14c, Supporting Information). As mentioned above, the fluorescence lifetime is related to the exciton diffusion and charge transfer processes. Here, all the obtained TR-PL decay curves were well fitted to a bi-exponential decay function (Figure S15, Supporting Information), consisting of the fast (τ_1) and slow (τ_2) lifetime components (Table S6, Supporting Information). For the PTB7:$PC_{71}BM$ JNP film, the PL decay time was shortened when a particular annealing treatment (140 °C, 10 min) was applied (Figure S14d, Supporting Information). The Janus NP film exhibited a much shorter fluorescence lifetime (0.319 ns) than the film without an annealing process (0.355 ns). It was consistent that 140 °C annealed NP film showed the more effective PL quenching and best photovoltaic performance as well.

As discussed above, the fast decay τ_1 is attributed to non-radiative decay, which originates from the charge extraction within the NP film; while, τ_2 is related to the radiative recombination of free charge carriers within the D:A NP film. After 140 °C annealing treatment, both τ_1 and τ_2 had dramatically shortened to 0.231 and 0.673 ns, respectively. It indicates the more efficient charge extraction after annealing treatment. Therefore, the post-thermal treatment improved the charge diffusion and transfer rate, resulting in the reduction of geminate charge recombination.

Last, we summarized the performance of D:A NP based organic photovoltaics in the past 20 years. Our assembled NP based solar cells exhibited the competitive performance (Table S7, Supporting Information).

3. Conclusion

In this work, we designed and controlled the morphology of interfacial arrays of organic donor:acceptor NPs comprising homogeneous core–shell and Janus internal structures into a close-packed monolayer. We studied the effect of the self-assembled and organized structures on photoelectronic behavior as well as device performance. Here, an interfacial self-assembly technique was introduced to prepare D:A NP films on a large scale (2×2 cm^2), using the spontaneous spreading phenomenon. With this approach, the D:A NPs were highly mobile at the air/water interface, and their assemblies could be densely packed in 1 min. The obtained NP films were successfully transferred onto various substrates, including flexible and patterned substrates.

Due to the internal phase separation, the Janus structure exhibits the benefit of making the photo-active layer more efficient for charge transfer and extraction. Therefore, the Janus NP device shows 80% higher electron mobility and more balanced charge transport than the traditional core–shell NP device. Consequently, the Janus NP film-based devices yield PCE 50% higher than traditional core–shell NP devices. Notably, the PTB7-Th:$PC_{71}BM$ Janus NPs exhibit highly efficient photovoltaic performances with over 5%, representing one of the best results in NP based organic photovoltaics. Our approach and results open a new road for the application of donor:acceptor Janus nanoparticle coatings in optoelectronic applications in the near future.

4. Experimental Section

Materials: Ethanol, 1-butanol, hexane, *N*-Methyl-2-pyrrolidone (NMP), chloroform, 1,2-dichlorobenzene (o-DCB), acetone, isopropyl alcohol (IPA), sodium dodecyl sulfate (SDS), and zinc oxide (ZnO) nanoparticles (2.5 wt% in 2-propanol, diluted to 1 wt%, Nanograde, N-10) were obtained from Sigma–Aldrich. Poly [[4,8-bis[(2-ethylhexyl) oxy]benzo[1,2-b:4,5-b"]dithiophene-2,6-diyl][3-fluoro-2-[(2-ethylhexyl) carbonyl]thieno[3,4-b]thiophenediyl]] (PTB7), Poly[4,8-bis(5-(2-ethylhexyl) thiophen-2-yl)benzo[1,2-b;4,5-b"]dithiophene-2,6-diyl-alt-(4-(2-ethylhexyl)-3-fluorothieno[3,4-b]thiophene-)-2-carboxylate-2-6-diyl)] (PTB7-Th), and [6,6]-Phenyl-C_{71}-butyric acid methyl ester ($PC_{71}BM$, >99%) were purchased from Ossila Ltd. Deionized water (DI water) was used in aqueous experiments. All these chemicals were used as received without any purification.

Synthesis of Pure Donor and Acceptor NP Dispersions: The synthesis process of PTB7 or $PC_{71}BM$ NPs was introduced in the authors' previous work.[31] Briefly, 5 mg of PTB7 or 5 mg of $PC_{71}BM$ was dissolved in 1 mL of chloroform with continuous stirring at 50 °C overnight. Then, 5 mL SDS solution (34.7 mM) in deionized water was rapidly injected into the organic solution. The two mixed solutions were vigorously stirred and then directly ultrasonicated at 240 W for 2 min. The resulting blend was heated at 61 °C through a water bath to evaporate chloroform.

Synthesis of Acceptor-Core:Donor-Shell NP Dispersions: 5 mg PTB7 (PTB7-Th) and 5 mg $PC_{71}BM$ were first dissolved in 2 mL of chloroform. Then, 10 mL SDS solution (34.7 mM) in deionized water was rapidly injected into the organic solution under stirring. The two mixed solutions were vigorously stirred and then directly sonicated at 240 W for 2 min. The resulting blend was heated at 61 °C through a water bath to evaporate chloroform.

The residual surfactants from the NP dispersion were removed by using Amicon ultra-6 centrifuge filter (cutoff 100K) at 3000 rpm for 20 min for each dialysis. This procedure was repeated eight times before assembly experiments.

Synthesis of Donor:Acceptor Janus NP Dispersions: 8 mL of freshly prepared core–shell NPs colloid was transferred to a 20 mL vial with stirring at room temperature at 650 rpm. Then, 2 mL NMP was rapidly injected into the vial and further stirred for 30 min. The blend was transferred in centrifugal dialysis tubes (100 kDa molecular weight cutoff) to start the centrifugal dialysis (3000 rpm, 20 min). This step was aimed at removing the mixed NMP. After the centrifugal dialysis, the dispersion was refilled with fresh DI-water. This procedure was repeated five times to obtain Janus NPs.

Float Assembly of Donor:Acceptor NPs at the Air/Water Interface: The NP dispersion (0.25 mL, 1 mg mL^{-1}) and dispersed solvents (0.25 mL) were well mixed after 1 min ultrasonic. When the NPs were mixed with ethanol or IPA, the filter process could be applied before adding the dispersion to water. The mixture was dropped slowly at the center of the container filled with DI water (diameter of 5 cm) using a pipette. The volume of each component could vary according to the size of the container. After the injection, a few drops of 1-butanol were dropped at the edge of the container to induce close-packing nanoparticle arrays. The obtained NP films were transferred onto various substrates for further characterization and applications. The films were again

washed in the water-ethanol mixture (50:50 v/v) to remove the excess surfactant. Before that, the NP films were annealed at 140 °C for 10 min to avoidredispersion.

Assembly of Donor:Acceptor NPs at the Hexane/Water Interface: A few amounts of hexane were dropped on the water surface to generate an oil/water interface. Then, the mixed NP dispersion with butanol was injected slowly at the hexane/water interface using a syringe with a needle. After several min, the hydrophobic solvent evaporated, leaving the nanoparticle film on the water surface.

Fabrication of Polymer Solar Cells (PSCs): In general, pre-patterned indium tin oxide (ITO) substrates were cleaned with detergent (Decon-90), boiling DI-water, acetone, boiling DI-water, and isopropanol through an ultrasonic bath for 15 min each. After drying, the substrates were cleaned with UV-ozone treatment (20 min). The zinc oxide (ZnO) NPs (2.5 wt% in 2-propanol, diluted to 1 wt%, Nanograde, N-10) layer was deposited on substrates through spin-coating (3000 rpm, 30 s). Then, the substrates were annealed at 150 °C for 10 min under the N_2 atmosphere. The resulting substrates were then treated with N_2-plasma for 20 s. Then, the prepared donor:acceptor NPs film was transferred onto the annealed ZnO layer and dried on a hot plate (80 °C) and annealed at different temperatures for 10 min. For bulk heterojunction (BHJ) devices, the photo-active layer was spin-coated from DCB solution (20 mg mL^{-1}, 2000 rpm, 60 s) under the ambient condition. Last, the MoO_3 (5 nm) and Ag (75 nm) were thermally evaporated (5.0×10^{-6} mbar) through a shadow mask, resulting in the photo-active area of solar cells as 8×4.0 mm^2. The obtained devices were stored under the ambient condition for further stability measurement.

Fabrication of Electron-Only and Hole-Only Devices: The architecture of electron-only devices was glass/ITO/ZnO/NP layer (80 nm) / aluminum (Al) (100 nm). The architecture of hole-only devices was glass/ITO/MoO_3 (80 nm)/NP layer/MoO_3 (5 nm)/Ag (75 nm). The fabrication method and procedure were the same as solar cells. The NP layer was annealed at 140 °C for 10 min before space-charge-limited current (SCLC) measurement.

Characterization: *Transmission Electron Microscopy (TEM)*: TEM images in this work were obtained from a Zeiss Libra120 electron microscope under the operating voltage of 120 kV. The energy-filtered TEM images (EF-TEM) were recorded using an Omega-type energy filter. For mapping carbon and sulfur elements, the standard three-windows EF-TEM method with a slit width of 20 eV and the energy windows of 240, 268, 303, 131 eV, 153, and 200 eV were used, respectively. The film samples were prepared by transferring the floating NP film from the water surface onto copper grids.

Scanning Electron Microscopy (SEM): The surface morphology of donor:acceptor NP films was measured using a Zeiss SEM NEON 40 EsB CrossBeam in the in-lens mode with an accelerating voltage of 3.0 kV. The samples of donor:acceptor NP films were prepared by transferring the floating NP films onto highly doped silicon substrates. The samples were coated with platinum (3.0 nm) utilizing a Leica SCD500 sputter coater to prevent charging.

Contact Angle Measurement: The wetting properties of the surfaces were characterized by a measurement system (OCA 35xl, DataPhysics Instruments GmbH, Germany). A 10 µL water droplet was used for each surface, and measurements were performed at five different positions for each sample to obtain the average water contact angle.

Surface Tension: A multi-functional tensiometer analyzed the equilibrium surface tension (γ) using the pendant drop method. The droplets were recorded as videos with a high-speed camera native to the tensiometer. The morphology variation of the liquid by jetting an aqueous phase in the air was captured by using a high-speed camera (OCA 35xl, DataPhysics Instruments GmbH, Germany). Every sample was repeated at least five times to obtain the average surface tension.

UV–Vis Absorption: The D:A NP films were transferred to the quartz glass for UV–vis absorption measurement. At room temperature, the UV–vis absorption spectra were measured on an Agilent Cary 5000 UV–vis–NIR spectrophotometer.

Steady-State Photoluminescence (PL) Spectra: The PL spectra in this work were recorded on a PerkinElmer LS-55. The excitation wavelength was set to 405 nm. The D:A NP films were transferred to the quartz glass for this PL measurement.

Time-Resolved Photoluminescence (TR-PL): TR-PL was measured by a time-correlated single-photon counting (TCSPC) technique on a Microtime-200 system (PicoQuant, Germany) with a 100× air objective (UPLFLN, NA 0.9, Olympus, Japan). For excitation, a picosecond pulsed p-polarized laser diode source (LDH-D-C-405, PicoQuant, Germany) with a center wavelength of 405 nm and a pulse width of 110 ps (full width at half maximum, FWHM), driven at a repetition rate of 0.5 MHz was used. For fluorescence collection, a dichroic mirror (ZT405-442/510rpc-UF3, Chroma, USA), a long pass filter with a cutoff below 425 nm (FF01-519/LP, Shamrock, USA), and a single photon counting module (SPCM-AQRH, Excelitas, USA) were used. For evaluation, SymphoTime 64 2.3 was used. PL lifetime images were recorded at 1 µW excitation power (before the objective) and a dwell time of 2 ms per pixel. TCSPC experiments were performed at 0.2 µW excitation power (before objective) and a measurement time of 60 s. The instrument response function (IRF) was collected at the same excitation conditions and recalculated from the TCSPC measurements. For TR-PL measurements, the nanoparticle films were transferred to quartz coated slides.

Current Density–Voltage (J–V) Characteristics: In this work, the performance of the solar cell devices was characterized by TriSol solar simulator (OAI, United States) with 300 W Xenon lamp under AM1.5 illumination. Under ambient conditions, the light current density–voltage curves were recorded with a source meter (110-1A, OAI, United States). The light source calibration was achieved by using a silicon-based reference cell. The dark *J–V* characteristics were obtained without illumination. All the devices were measured in ambient air.

Space-Charge-Limited-Current (SCLC): The dark *J–V* characteristics were measured for electron-only and hole-only devices. The architecture of hole-only devices was glass/ITO/MoO_3 (5 nm)/NP layer/MoO_3 (5 nm)/Ag (75 nm). The architecture of electron-only devices was glass/ITO/ZnO/NP layer/Al (100 nm).

Supporting Information

Supporting Information is available from the Wiley Online Library or from the author.

Acknowledgements

The authors thank Dishi Wang for steady-state photoluminescence measurements, Dr. Binyu Zhao for contact angle measurements, and Dr. Tobias König, Olha Aftenieva for introduction into time-correlated single-photon counting (TCSPC) measurements. A.S. acknowledges the support from the DFG funding (SY125/15-1). V.S. acknowledges the support from the DFG funding (SFB-1415, No. 417590517). Y.D. acknowledges the financial support from the China Scholarship Council (CSC).

Open access funding enabled and organized by Projekt DEAL.

Conflict of Interest

The authors declare no conflict of interest.

Data Availability Statement

Research data are not shared.

Keywords

air/water interface, charge transfer, close-packed monolayer, donor:acceptor Janus nanoparticles, optoelectronic applications, self-assembly

Received: November 8, 2022
Revised: March 6, 2023
Published online: April 3, 2023

[1] R. Søndergaard, M. Hösel, D. Angmo, T. T. Larsen-Olsen, F. C. Krebs, *Mater. Today* **2012**, *15*, 36.
[2] D. Dang, D. Yu, E. Wang, *Adv. Mater.* **2019**, *31*, 1807019.
[3] S. Lee, D. Jeong, C. Kim, C. Lee, H. Kang, H. Y. Woo, B. J. Kim, *ACS Nano* **2020**, *14*, 14493.
[4] X. Xu, G. Zhang, L. Yu, R. Li, Q. Peng, *Adv. Mater.* **2019**, *31*, 1906045.
[5] H. Zhang, H. Yao, W. Zhao, L. Ye, J. Hou, *Adv. Energy Mater.* **2016**, *6*, 1502177.
[6] S. Dong, K. Zhang, B. Xie, J. Xiao, H. L. Yip, H. Yan, F. Huang, Y. Cao, *Adv. Energy Mater.* **2019**, *9*, 1802832.
[7] A. Holmes, E. Deniau, C. Lartigau-Dagron, A. Bousquet, S. Chambon, N. P. Holmes, *ACS Nano* **2021**, *15*, 3927.
[8] M. Rammal, P. Lévêque, G. Schlatter, N. Leclerc, A. Hébraud, *Mater. Chem. Front.* **2020**, *4*, 2904.
[9] S. Gärtner, A. J. Clulow, I. A. Howard, E. P. Gilbert, P. L. Burn, I. R. Gentle, A. Colsmann, *ACS Appl. Mater. Interfaces* **2017**, *9*, 42986.
[10] J. Kosco, M. Bidwell, H. Cha, T. Martin, C. T. Howells, M. Sachs, D. H. Anjum, S. G. Lopez, L. Zou, A. Wadsworth, *Nat. Mater.* **2020**, *19*, 559.
[11] J. Kosco, S. Gonzalez-Carrero, C. T. Howells, W. Zhang, M. Moser, R. Sheelamanthula, L. Zhao, B. Willner, T. C. Hidalgo, H. Faber, *Adv. Mater.* **2022**, *34*, 2105007.
[12] A. Liu, L. Gedda, M. Axelsson, M. Pavliuk, K. Edwards, L. Hammarström, H. Tian, *J. Am. Chem. Soc.* **2021**, *143*, 2875.
[13] J. Kosco, S. Gonzalez-Carrero, C. T. Howells, T. Fei, Y. Dong, R. Sougrat, G. T. Harrison, Y. Firdaus, R. Sheelamanthula, B. Purushothaman, *Nat. Energy* **2022**, *7*, 340.
[14] J. Cho, K. H. Cheon, H. Ahn, K. H. Park, S. K. Kwon, Y. H. Kim, D. S. Chung, *Adv. Mater.* **2015**, *27*, 5587.
[15] A. Rahmanudin, R. Marcial-Hernandez, A. Zamhuri, A. S. Walton, D. J. Tate, R. U. Khan, S. Aphichatpanichakul, A. B. Foster, S. Broll, M. L. Turner, *Adv. Sci.* **2020**, *7*, 2002010.
[16] L. Feng, P.-Q. Bi, X.-Y. Yang, M.-S. Niu, K.-N. Zhang, F. Wang, C.-K. Lv, Z.-C. Wen, X.-T. Hao, *Org. Electron.* **2018**, *57*, 140.
[17] C. Xie, A. Classen, A. Späth, X. Tang, J. Min, M. Meyer, C. Zhang, N. Li, A. Osvet, R. H. Fink, *Adv. Energy Mater.* **2018**, *8*, 1702857.
[18] C. Xie, T. Heumüller, W. Gruber, X. Tang, A. Classen, I. Schuldes, M. Bidwell, A. Späth, R. H. Fink, T. Unruh, *Nat. Commun.* **2018**, *9*, 5335.
[19] Y. J. Kim, R. D. Schaller, H. C. Fry, *Small* **2019**, *15*, 1803563.
[20] F. J. Colberts, M. M. Wienk, R. A. Janssen, *ACS Appl. Mater. Interfaces* **2017**, *9*, 13380.
[21] D. Liu, W. Cai, M. Marin, Y. Yin, Y. Li, *ChemNanoMat* **2019**, *5*, 1338.
[22] S. Shi, T. P. Russell, *Adv. Mater.* **2018**, *30*, 1800714.
[23] I. Langmuir, *Trans. Faraday Soc.* **1920**, *15*, 62.
[24] G. D. Moon, T. I. Lee, B. Kim, G. Chae, J. Kim, S. Kim, J.-M. Myoung, U. Jeong, *ACS Nano* **2011**, *5*, 8600.
[25] J. J. Giner-Casares, J. Reguera, *Nanoscale* **2016**, *8*, 16589.
[26] D. Liu, C. Li, F. Zhou, T. Zhang, G. Liu, W. Cai, Y. Li, *Adv. Mater. Interfaces* **2017**, *4*, 1600976.
[27] P. Gao, J. He, S. Zhou, X. Yang, S. Li, J. Sheng, D. Wang, T. Yu, J. Ye, Y. Cui, *Nano Lett.* **2015**, *15*, 4591.
[28] J. Li, Y. Hu, L. Yu, L. Li, D. Ji, L. Li, W. Hu, H. Fuchs, *Small* **2021**, *17*, 2100724.
[29] Y. Wang, M. Zhang, Y. Lai, L. Chi, *Nano Today* **2018**, *22*, 36.
[30] K. Landfester, *Angew. Chem., Int. Ed.* **2009**, *48*, 4488.
[31] Y. Du, Y. Li, O. Aftenieva, T. Tsuda, P. Formanek, T. A. König, A. Synytska, *Adv. Opt. Mater.* **2022**, *10*, 2101922.
[32] H. Wang, W. Chen, B. Chen, Y. Jiao, Y. Wang, X. Wang, X. Du, Y. Hu, X. Lv, Y. Zeng, *Small* **2020**, *16*, 1905480.
[33] D. F. Swinehart, *J. Chem. Educ.* **1962**, *39*, 333.
[34] M. L. Myrick, M. N. Simcock, M. Baranowski, H. Brooke, S. L. Morgan, J. N. McCutcheon, *Appl. Spectrosc. Rev.* **2011**, *46*, 140.
[35] Y.-K. Park, S.-H. Yoo, S. Park, *Langmuir* **2007**, *23*, 10505.
[36] Y.-K. Park, S. Park, *Chem. Mater.* **2008**, *20*, 2388.
[37] Y.-K. Park, S.-H. Yoo, S. Park, *Langmuir* **2008**, *24*, 4370.
[38] V. Sashuk, K. Winkler, A. Zywocinski, T. Wojciechowski, E. Gorecka, M. Fiałkowski, *ACS Nano* **2013**, *7*, 8833.
[39] T. Udayabhaskararao, T. Altantzis, L. Houben, M. Coronado-Puchau, J. Langer, R. Popovitz-Biro, L. Liz-Marzán, L. Vuković, P. Král, S. Bals, R. Klajn, *Science* **2017**, *358*, 514.
[40] J. Zhang, Y. Sun, R. Feng, W. Liang, Z. Liang, W. Guo, I. Abdulhalim, J. Qu, C. W. Qiu, L. Jiang, *Nanoscale* **2019**, *11*, 23058.
[41] K. M. Sim, S. Yoon, S.-K. Kim, H. Ko, S. Z. Hassan, D. S. Chung, *ACS Nano* **2019**, *14*, 415.
[42] Z. Zheng, J. Wang, P. Bi, J. Ren, Y. Wang, Y. Yang, X. Liu, S. Zhang, J. Hou, *Joule* **2022**, *6*, 171.
[43] P. W. Liang, C. Y. Liao, C. C. Chueh, F. Zuo, S. T. Williams, X. K. Xin, J. Lin, A. K. Y. Jen, *Adv. Mater.* **2014**, *26*, 3748.
[44] Y. Li, L. Meng, Y. M. Yang, G. Xu, Z. Hong, Q. Chen, J. You, G. Li, Y. Yang, Y. Li, *Nat. Commun.* **2016**, *7*, 10214.
[45] Y. J. Kim, P. Guo, R. D. Schaller, *J. Phys. Chem. Lett.* **2019**, *10*, 6525.
[46] V. Mihailetchi, J. Wildeman, P. Blom, *Phys. Rev. Lett.* **2005**, *94*, 126602.
[47] T. Kumari, S. M. Lee, C. Yang, *Adv. Funct. Mater.* **2018**, *28*, 1707278.
[48] H. Zhou, Y. Zhang, J. Seifter, S. D. Collins, C. Luo, G. C. Bazan, T. Q. Nguyen, A. J. Heeger, *Adv. Mater.* **2013**, *25*, 1646.
[49] D. Leman, M. A. Kelly, S. Ness, S. Engmann, A. Herzing, C. Snyder, H. W. Ro, R. J. Kline, D. M. DeLongchamp, L. J. Richter, *Macromolecules* **2015**, *48*, 383.